Effect of particle size distribution on the laminar flame speed of iron aerosols

Combustion and Flame 257 (2023) 113053

Contents lists available at ScienceDirect

Combustion and Flame

journal homepage: www.elsevier.com/locate/combustflame

Effect of particle size distribution on the laminar flame speed of iron aerosols

Aravind Ravi*, Philip de Goey, Jeroen van Oijen

Mechanical Engineering, Eindhoven University of Technology, the Netherlands

ARTICLE INFO

Article history:
Received 9 January 2023
Revised 23 August 2023
Accepted 28 August 2023

Keywords:
Metal combustion
Particle size distribution
Heterogeneous combustion
Laminar flame speed
Iron aerosols

ABSTRACT

Iron particles in air burn in heterogeneous combustion mode and the flame speed is very sensitive to particle size. Previous numerical work on the propagation of flames in iron dust was based on average particle sizes. However, in practice, experiments are conducted with particle size distributions (PSD). This makes it challenging to compare different experiments as the samples used in those studies vary (the average particle size might be similar but not the particle size distribution). It is the aim of the current work to provide insight into the effect of particle size distribution on flame propagation. This involves identifying the minimum number of discrete averaged particle sizes (bins) required in the simulations to capture the burning characteristics of the PSD. Then, flame speed and flame structure for a narrow and broad distribution are investigated. It is shown that the equivalence ratio at which the maximum flame speed occurs for certain mean particle sizes varies with the width of the particle size distribution. The difference in the flame speed between the same average particle size but different standard deviation varies as a function of β (ratio between standard deviation and average particle size), not just the average particle size itself. For a constant β at a particular equivalence ratio, the difference in the flame speed between PSD and mono-dispersed aerosols is approximately the same irrespective of the particle size. The effects of the smaller and bigger particles in the PSD on the flame speed and flame structure are also systematically investigated. The findings in this study confirm that the particle width of the PSD plays a crucial role and that experiments and simulations can not be readily compared if different PSDs are used.

1. Introduction

Alternative fuels with no or fewer carbon dioxide emissions are currently being explored to reduce our dependency on fossil fuels. One of the promising alternative fuels is iron, especially iron with particle sizes in the order of microns. Iron has a high energy density and a low specific volume compared to fossil fuels. Also, burning iron does not produce carbon dioxide and the burned product can be captured and recycled using renewable sources [1].

Iron particle size, concentration, and morphology influence flame propagation and flame structure. Most of the conclusions about the flame speed of iron aerosols were reported as a function of average particle sizes [2–5] and hence cannot be compared directly with other experimental and theoretical results. In reality, each particle sample has its own particle size distribution (PSD) and standard deviation which can result in different flame speeds and flame structures even if the average particle size was kept the same.

To understand the effect of different reaction times of two different fuels and different sizes of the same fuel, the combustion of a binary suspension of two mono-size powders was investigated by Goroshin et al. [3] with the assumption of constant ignition temperature in the binary mixture for two different particle sizes and fuels. They postulated that various flame front configurations can be observed in the binary dispersed mixture. A similar analysis was performed by Palecka et al. [5] in binary fuel mixtures and hypothesized similar results by Goroshin et al. [3].

In the work of Hazenberg and van Oijen [6] a numerical model for the propagation of iron flames is developed, using this model they showed that the maximum flame speed is expected to be at lean conditions for mono-dispersed iron aerosols. More recently, this work was extended by Aravind et al. [7] to simulate binary suspensions. Again, the observations of Goroshin et al. [3] were confirmed; different flame fronts can occur depending on the particle size ratio. But it was also found that the fuel equivalence ra-

* Corresponding author.
E-mail address: a.ravi@tue.nl (A. Ravi).

https://doi.org/10.1016/j.combustflame.2023.113053

tio at which maximum flame speed occurs shifted from lean conditions towards rich conditions as the difference in particle sizes increased. In this work, we are going to extend this study and perform a detailed analysis of the impact of particle size distributions on flame propagation to be able to evaluate the influence of different PSDs on flame structure and speed.

Section 2 explains the particle and gas-phase modeling along with its validation. Section 2 also shows the calculation of the effect of discrete particle sizes for the PSD. Section 3 shows the effect of the number of bins, and Section 4 explains the effect of standard deviation on the flame speed and structure. Section 5 shows the investigation of the effect of the small and big particles in the PSD respectively.

2. Methodology

A brief description of the particle and gas-phase modeling is presented here considering a heterogeneous combustion mode. For a detailed model please refer to Hazenberg et al. [6] and Aravind et al. [7].

2.1. Particle and gas-phase modeling

The reaction mechanism is assumed to be governed by a single-step reaction where the iron is converted to FeO:

$$\mathrm{Fe} + \frac{1}{2}\mathrm{O_2} \longrightarrow \mathrm{FeO} \tag{1}$$

and the mass-based stoichiometric ratio (s) is given by

$$s = \frac{\frac{1}{2}M_{\mathrm{O_2}}}{\mathrm{M_{Fe}}} = 0.2865 \tag{2}$$

where $M_{\mathrm{O_2}}$ and M_{Fe} are the molecular weight of oxygen and iron respectively. In previous studies [6,7], either one or two different particle sizes were tracked but here multiple particle sizes are tracked using the Lagrangian approach. Drag forces are calculated to find the time response of the particle velocity in relation to the gas flow. As the kinetic reaction is assumed to occur on the particle surface, and the oxide remains in a condensed phase, the volume of the particle increases and the particle volume is computed considering both the density of iron and iron oxide. With the assumption of a spherical particle, the diameter of the particle is computed from the volume of the particle. Using a mixture-averaged diffusion coefficient, the diffusion flux of oxygen to the particle's surface can be computed. Vapor-phase combustion of iron particles might occur at relatively large particle temperature [8] but the effect on the flame speed is marginal and hence excluded in our model. The oxidation process after the initial formation of FeO to Fe_2O_3 and Fe_3O_4 is slow and does not play an important role in the flame propagation and is also neglected.

A quasi-steady state between oxygen diffusion and the surface reaction rate is assumed to find the oxidizer concentration at the particle surface, which yields the surface reaction rate [9]. Both kinetic rates and diffusion rates are included in our model and the transition from kinetically controlled to diffusion-controlled combustion is handled by our model. The kinetic rate parameters are calibrated to have a particle ignition temperature as predicted by Breiter et al. [10].

For the gas phase, mass, species conservation, and energy equations are considered. Only the exchange of oxygen has to be considered for the species conservation equation as oxygen is consumed by the iron particles. The system of equations is implemented in the finite-volume 1D flame solver CHEM1D [11,12]. The coupling between the particle modeling and the gas phase modeling follows a similar methodology as in Sacomano Filho et al. [12].

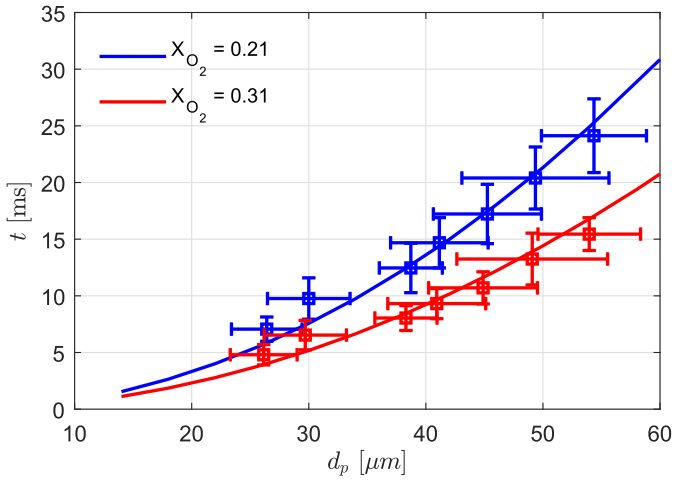

Fig. 1. Time taken to reach maximum temperature for different particle sizes (blue line for $X_{\mathrm{O_2}} = 0.21$ and red line for $X_{\mathrm{O_2}} = 0.31$) compared against experimental results (symbols) from Ning et al. [8]. (For interpretation of the references to colour in this figure legend, the reader is referred to the web version of this article.)

2.2. Validation of the particle model

While the particle model was validated against experiments performed by Ning et al. [8] in our previous study [7], we present here an update with modified initial conditions. Instead of an initial particle temperature of $T_p = 1700\,\mathrm{K}$ we use $T_p = 1100\,\mathrm{K}$. Figure 1 (left) shows the time taken by the particle to reach maximum temperature ($t_{b,\max}$) at a gas temperature of $T_g = 300\,\mathrm{K}$ and initial particle temperature of $T_p = 1100\,\mathrm{K}$ in air for two different oxygen concentrations in air ($X_{\mathrm{O_2}} = 0.21$ and $X_{\mathrm{O_2}} = 0.31$). The $t_{b,\max}$ is calculated from when the temperature of the particle reaches $T_p = 1500\,\mathrm{K}$ to a maximum temperature, similar to the method followed in other studies [13,14]. The $t_{\mathrm{b,max}}$ computed using our numerical model is in line with the experimental results for both oxygen concentrations and various particle sizes and this serves as a validation of our current particle model.

The maximum particle temperature reported by Ning et al. [8] is almost constant for different particle sizes considering oxygen concentrations of 21% or lower. The maximum temperature of a particle computed using our model for $d_{\mathrm{p,avg}} = 26$ µm and $d_{\mathrm{p,avg}} = 50$ µm are 2180 K and 2210 K at the oxygen concentration of 21% respectively. These predicted values are very close to the experimentally obtained maximum particle temperatures of 2150 K from Ning et al. [8] for the same particle sizes and oxygen concentration. Experimentally obtained maximum particle temperature values are within ±150 K for different particle sizes which indicates that the maximum temperature particle hardly depends on particle size for these conditions. When considering particles burning in lower oxygen concentrations, as it is the case in iron flames, the maximum particle temperature is almost constant for different particle sizes [8].

In previous work [14], it was found that the temperature of a single iron particle burning in air can become as high as 2500 K, resulting in a small fraction of Fe vaporization. At an oxygen concentration of 21%, the corresponding fraction of iron that evaporates was found to be the order of one percent, and this fraction decreased with decreasing oxygen level. In the flames investigated here, the particles burn in an environment with relatively low oxygen concentration, and their temperatures remain low enough to prevent significant evaporation of iron. Therefore, we have assumed that the particle conversion rate and hence the flame speed are mostly dominated by heterogeneous combustion of iron particles.

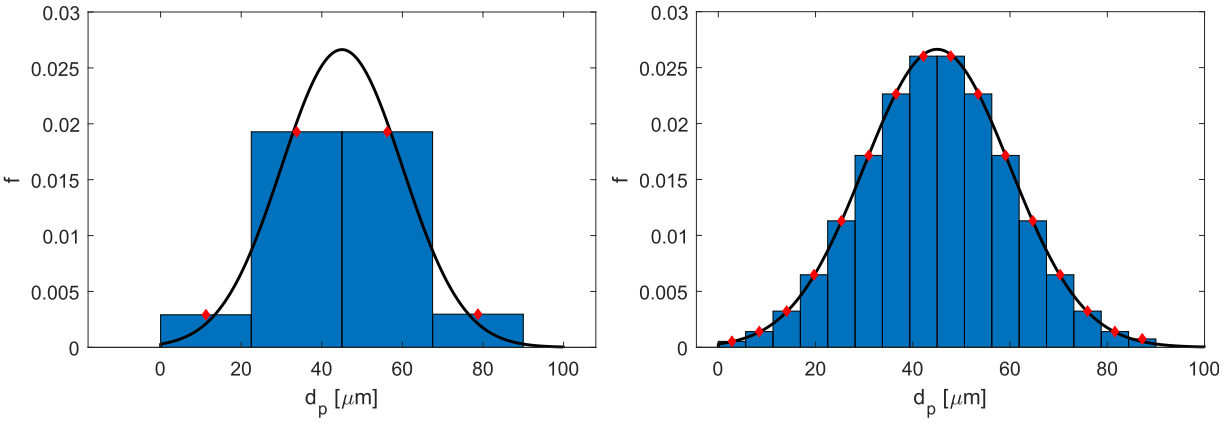

Fig. 2. Normal particle distribution represented by 4 bins (left) and 16 bins (right) for $d_{\mathrm{p,avg}} = 45$ µm with $\sigma = 15$ µm.

Table 1
Discrete particle diameters and their distribution functions for distribution with $d_{\mathrm{p,avg}} = 45$ µm and $\sigma = 15$ µm and $n_d = 4$.

i	$d_{\mathrm{p,i}}$ (µm)	y_i	f_i (µm^{-1})
1	11.25	0.066	0.0029
2	33.75	0.434	0.0193
3	56.25	0.434	0.0193
4	78.75	0.066	0.0029

2.3. Discrete particle sizes to represent PSD

The particle size distribution of a certain powder can be characterized by the cumulative mass distribution function $F(d_{\mathrm{p}})$, which gives the mass fraction of particles with a diameter smaller than or equal to d_{p}. In order to use this continuous distribution function in CHEM1D, it needs to be represented by a discrete number n_d of particle diameters $d_{\mathrm{p},i}$ with $i = 1, \ldots, n_d$. The mass fraction y_i of each discrete particle size is then determined by computing the mass fraction of all particles in the range from $d_{\mathrm{p},i-1/2}$ to $d_{\mathrm{p},i+1/2}$:

$$y_i = F(d_{\mathrm{p},i+1/2}) - F(d_{\mathrm{p},i-1/2}) \tag{3}$$

where $d_{\mathrm{p},i+1/2} = \frac{1}{2}(d_{\mathrm{p},i} + d_{\mathrm{p},i+1})$, the arithmetic mean of two neighbouring diameters. The extreme boundaries for the first and last range are $d_{\mathrm{p},1/2} = 0$ and $d_{\mathrm{p},n_d+1/2} = \infty$, respectively, such that all particle sizes are included.

In this study, we consider particle size distributions that have a normal distribution. Their cumulative distribution function is given by the error function

$$F(d_{\mathrm{p}}) = \mathrm{erf}\left(\frac{d_{\mathrm{p}} - d_{\mathrm{p,avg}}}{\sqrt{2}\sigma}\right) \tag{4}$$

with $d_{\mathrm{p,avg}}$ the mean and σ the standard deviation. Since negative particle diameters are not physical, the part with $d_{\mathrm{p}} < 0$ is ignored and the distribution function is re-normalized

$$F'(d_{\mathrm{p}}) = \frac{F - F(0)}{1 - F(0)} \tag{5}$$

such that $F'(0) = 0$. From here on the prime will be dropped and the re-normalized distribution function will be simply denoted by F.

These continuous normal distributions will be represented by discrete particle sizes $d_{\mathrm{p},i}$ that are equally spaced between $d_{\mathrm{p},1/2} = d_{\mathrm{p,avg}} - 3\sigma$ and $d_{\mathrm{p},n_p+1/2} = d_{\mathrm{p,avg}} + 3\sigma$. The minimum diameter should of course be larger than zero and is limited in this study to 1 µm. The distribution function f_i of the discrete set of particle sizes is calculated as,

$$f_i = \frac{y_i}{d_{\mathrm{p},i+1/2} - d_{\mathrm{p},i-1/2}} \tag{6}$$

As an example, Fig. 2 shows the continuous and discrete distribution functions with $d_{\mathrm{p,avg}} = 45$ µm and $\sigma = 15$ µm for $n_d = 4$ and $n_d = 16$. The discrete particle diameters and their mass fractions (y_i) and distribution function (f_i) are listed in Table 1 for $n_d = 4$. In Fig. 2 the chosen discrete particle sizes are highlighted (diamond symbol) on the normal distribution curve and shown as a bin with constant width for visualization.

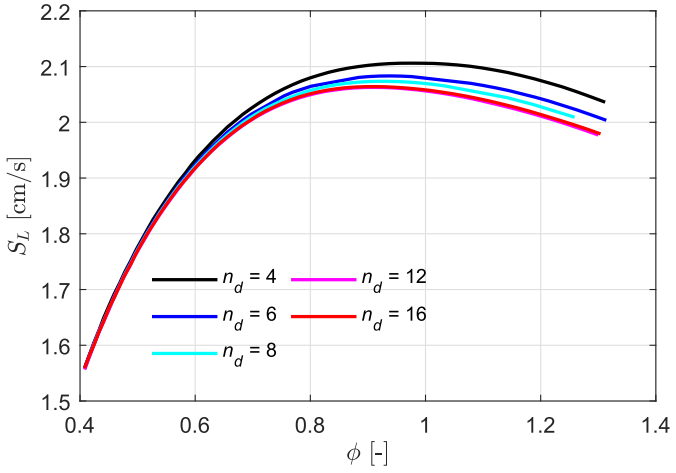

Fig. 3. Flame speed for different number of bins (n_d) against equivalence ratio for $d_{\mathrm{p}} = 45$ µm with $\sigma = 15$ µm.

3. Effect of number of bins

A particle size distribution represented with a very large number of discrete particle sizes (bins) needs more computational time. Also, choosing a very low number of bins may not represent the original PSD well. Hence, finding the number of bins required to completely capture the PSD behavior is crucial, which means that when the number of bins changes, the results should not change significantly.

Figure 3 shows the flame speed (S_L) as a function of ϕ with a different number of bins for $d_{\mathrm{p,avg}} = 45$ µm with $\sigma = 15$ µm. For lean conditions ($\phi = 0.4$ to 0.7), the number of bins hardly affects the flame speed. The number of bins starts to affect the flame speed when $\phi > 0.7$ with slightly higher S_L for lower n_d. Figure 4 shows the temperature profiles of the gas and different

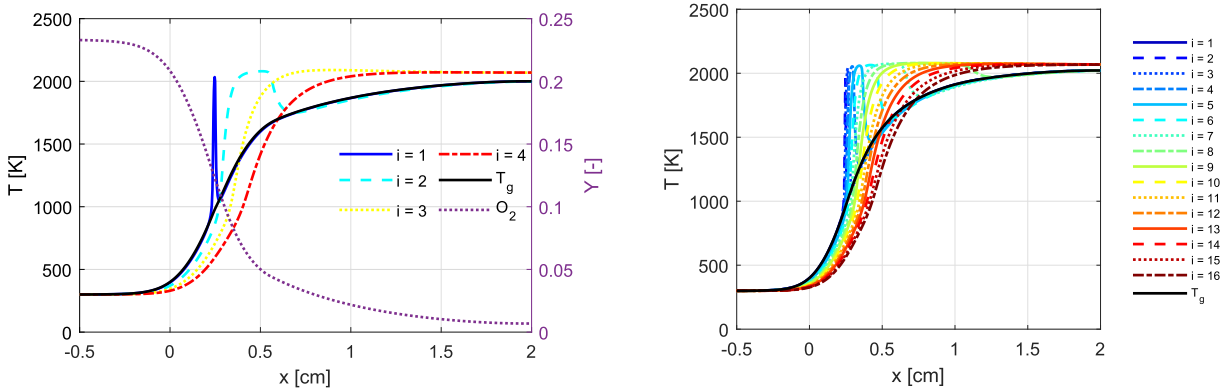

Fig. 4. Temperature of the gas and particles of different diameter for $d_{\mathrm{p,avg}} = 45$ µm and $\sigma = 15$ µm for 4 bins (left) and 16 bins (right) at $\phi = 1.2$. The colored profiles represent each particle size from 1 to n_d.

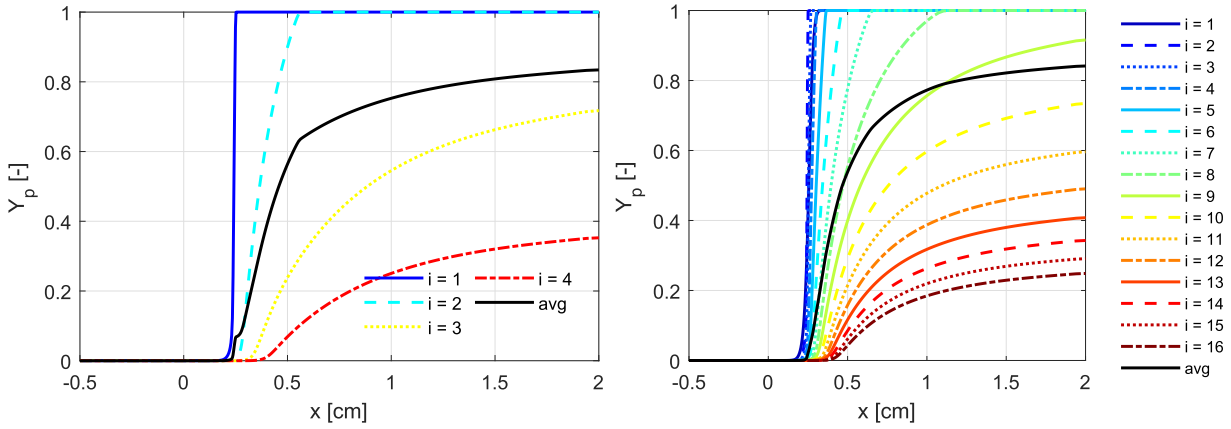

Fig. 5. Burned mass fraction profile for $d_{\mathrm{p,avg}} = 45$ µm and $\sigma = 15$ µm for 4 bins (left) and 16 bins (right) at $\phi = 1.2$. The colored profiles represent each particle size from 1 to n_d while the black line represents the mass-weighted average of all particle sizes.

particle sizes in the PSD for 4 bins (left) and for 16 bins (right) at $\phi = 1.2$ along with the amount of oxygen concentration. Notice that the amount of oxygen concentration available when the particle starts to burn is less than $Y_{\mathrm{O6_2}} = 0.14$ because of oxygen diffusion. The corresponding burned mass fraction ($Y_{\mathrm{p}} = m_{\mathrm{p,FeO}}/m_{\mathrm{p}}$) is shown in Fig. 5. When there are 4 different particle sizes, 2 out of 4 of the particle sizes reach the equilibrium gas temperature and burn completely (converted into iron oxide) within the computational domain, and when the number of bins is increased to $n_d = 16$, 8 out of 16 particle sizes reach the equilibrium temperature and burn completely for $\phi = 1.2$. Hence, half of the particle sizes (from $d_{\mathrm{p},1}$ to $d_{\mathrm{p},n_d/2}$) reaches thermal equilibrium and burns completely in the domain. Also, the averaged mass fraction of iron oxide ($Y_{\mathrm{p,avg}}$) calculated from each of the discrete particle sizes, $Y_{\mathrm{p,avg}} = \sum_1^{n_d} y_i Y_{\mathrm{p},i}$ is approximately the same (Fig. 5) for these two cases. But when looking at the actual particle sizes, i.e. when considering $n_d = 4$, the particle sizes that are completely burned are $d_{\mathrm{p},1} = 11.25$ µm and $d_{\mathrm{p},2} = 33.75$ µm and for $n_d = 16$, the particle sizes range from $d_{\mathrm{p},1} = 1.14$ µm and $d_{\mathrm{p},n_d/2} = d_{\mathrm{p},8} = 42.19$ µm, a very clear difference emerges. When the number of bins are lower (say $n_d = 4$) then the particle sizes (critical particle sizes and concentration) that influence the flame speed are 30% smaller than the average particle size but when the bins are increased (say $n_d = 16$) then the particle sizes that influence the flame speed are 10% smaller than the average particle size.

When the particle size ratio $d_{\mathrm{p},i}/d_{\mathrm{p},i+1} > 0.3$ then separated flame fronts prevail provided that there is a sufficient concentration of particles for flame propagation. When the particle size ratio $d_{\mathrm{p},i}/d_{\mathrm{p},i+1} \lesssim 0.3$, then overlapping flame fronts emerge. When a separated flame front exists, the flame speed is dominated by the burning of small particles in this flame front and the big particles merely burn in the post-flame region and take away heat from the flame. In the case of overlapping flame fronts, the flame speed is a combination of both small and big particles [7]. Hence, considering $n_d = 4$, the flame fronts are separated which is visible in Fig. 5 (left) as $Y_{\mathrm{p,avg}}$ shows a piece-wise behavior with sudden changes and for $n_d = 16$, the flame fronts are overlapping considering the smoother average profile of $Y_{\mathrm{p,avg}}$ in Fig. 5 (right). To conclude, because the particle sizes that are completely burned are smaller for $n_d = 4$ compared to $n_d = 16$, the flame speed is slightly higher for PSD with $n_d = 4$.

Figure 6 shows the flame speed ratio between poly- and monodispersions ($S_L^* = S_L/S_{L,\mathrm{mono}}$) against the number of bins for different dimensionless standard deviation $\beta = \sigma/d_{\mathrm{p,avg}}$ values and equivalence ratios. It is clear from Fig. 6 that S_L^* does not change much when the number of bins is increased. From a large number of simulations, it is found that the minimum number of bins required is $n_d \approx 12$ to have a difference in the flame speed of less than 2%. As σ increases, so does the difference in the size of the smallest and biggest particles in the distribution. The smallest particles burn faster and in doing this they increase the flame speed; this results in big particles not burning completely in the domain. Hence, increasing the number of bins to capture the burning characteristics of the biggest particles is not necessary and will not have a significant influence on flame speed. The effect of particle size ratio on the flame speed of binary dispersions was detailed in our previous work [7].

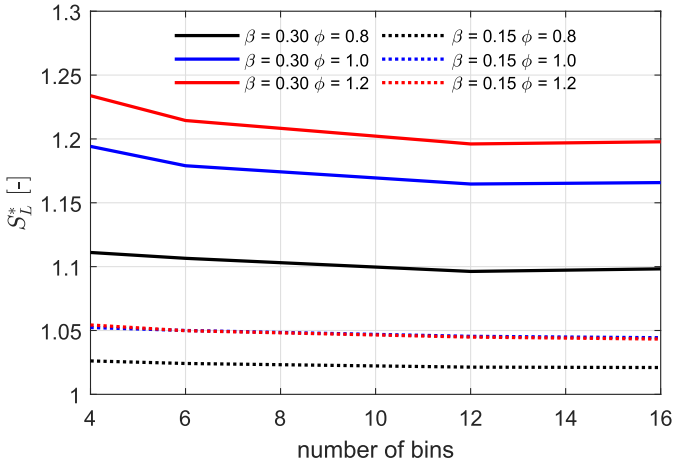

Fig. 6. $S_L^* = S_L/S_{L,\text{mono}}$ against number of bins at different β and ϕ.

4. Effect of standard deviation

Both broad PSD [15] and narrow PSD [16,17] were used in the experimental studies of iron combustion. Different experimental measurements were performed using different metal powders and each powder has a particle size distribution associated with it. Let us evaluate what happens when the standard deviation is varied for constant average particle size. Figure 7 shows the flame speed for the $d_{\text{p,avg}} = 45$ µm (left) and $d_{\text{p,avg}} = 20$ µm (right) at various σ compared against the mono-dispersed case as a function of equivalence ratio.

Let us first consider a broad distribution which includes very small (3.75 µm) as well as big particle sizes (86 µm) compared to the average particle size $d_{\text{p,avg}} = 45$ µm (and $\sigma = 15$ µm). Comparing $d_{\text{p,avg}} = 45$ µm with $\sigma = 15$ µm against the mono-dispersed case from Fig. 7 (left), for $\phi < 0.6$, the maximum difference in the flame speed is approximately 5%. At low equivalence ratios (say $\phi < 0.6$), almost all the particles in the poly-dispersed mixture are needed to have a self-sustainable flame front as the mass density of the smallest particle size ($d_{\text{p,1}}$) in the mixture is too low to have a stable flame front on its own. This is supported by Fig. 8 (left), which shows the temperature evolution of each discrete particle size at $\phi = 0.5$. Notice that all discrete particle sizes reach thermal equilibrium. Figure 9 (left) shows the burned mass fraction for each discrete particle size at $\phi = 0.5$ and all the particles are completely burned.

As ϕ increases (say $\phi = 0.8$) so does the mass density of small particles (as well as the total mixture density), which results in an increased flame speed as can be observed in Fig. 7. Figure 8 (right) shows the temperature evolution of each discrete particle size at $\phi = 1.0$. Figure 9 (right) shows the burned mass fraction for each discrete particle size at $\phi = 1.0$. As ϕ increases, there is a possibility that a fraction of the particles may not burn completely because they oxidize in the post-flame region and therefore they do not contribute to the flame speed.

An interesting observation in Fig. 8, is that the temperature of particles of different sizes is different in lean conditions but looks similar in rich conditions. In lean conditions, considering Fig. 8 (left), the peak temperatures of small particles are lower than big particles, as small particles heat up faster and burn when the surrounding gas temperature is relatively low. The temperature of the particle depends on heat production and heat loss rates. Small particles lose more heat than big particles as the surrounding gas temperature is lower when small particles are burning. In rich conditions, small particles take away the oxygen, and big particles are merely heated up to the gas temperature as the reaction rate is limited by kinetics [6]. As the particle temperatures in rich conditions are limited by the kinetics, we observe similar peak temperatures for all particle sizes in Fig. 8 (right) which is also explained in detail in previous studies [6,7]. In our model, peak particle temperatures are not limited by the thermal decomposition of iron oxide, which only happens at a much higher temperature (around 3700 K).

Comparing the flame structure of the mono-dispersed and poly-dispersed case, the increase in the gas temperature is more gradual in the poly-dispersed case as $d_{\text{p,1}}$ (smallest particle size in the PSD) burns first and then $d_{\text{p,2}}$ (next smallest particle size) starts to burn. If the size difference between $d_{\text{p,1}}$ and $d_{\text{p,2}}$ is very small (say $d_{\text{p,2}} < 1.3\, d_{\text{p,1}}$) both of them burn together (overlapping flame fronts) [7], otherwise they burn as a separated flame front. In Fig. 9, it can be seen that some of the big particle sizes start to burn after some of the small particle sizes are completely burned because the big particles need more time to heat up; this shows the different burning time scales when using a PSD. These different heating and burning time scales are responsible for the shift in $\phi_{S_{\text{L,max}}}$ as σ changes. In the mono-dispersed case, $\phi_{S_{\text{L,max}}} \approx 0.7$ and in the poly-dispersion the maximum flame speed occurs at $\phi_{\text{s,max}} \approx 0.9$ (for $d_{\text{p,avg}} = 45$ µm and $\sigma = 15$ µm). The value of $\phi_{S_{\text{L,max}}}$ in the poly-dispersed case is determined by the enhancement of the flame speed by the small particles and the heat taken away by the big particles. As small particles heat up and burn faster than big particles, the flame speed is largely controlled by the small particles if there is a sufficient amount of small particles to compensate for the heat loss to the big particles in the mixture. This is a significant finding as this shows the vulnerability of experimental results using different σ but the same $d_{\text{p,avg}}$. Consistent flame speed evaluation using an experimental setup may not be possible unless the PSD is known or kept relatively constant. This can explain why some experimental results show that the $\phi_{S_{\text{L,max}}}$ occurs at rich conditions [18] and in some other experiments $\phi_{S_{\text{L,max}}}$ occurs at stoichiometric or even lean conditions [19].

Figure 10 shows the normalized flame speed $S_L/S_{\text{L,max}}$ (left) and the flame speed ratio S_L^* (right) against equivalence ratio for two different cases ($d_{\text{p,avg}} = 50$ µm and $\sigma = 15$ µm and $d_{\text{p,avg}} = 20$ µm and $\sigma = 6$ µm) with the same $\beta = 0.3$. Even though the average particle size and standard deviations are different, the normalized flame speed results match each other as β is kept constant. Similarly, S_L^* closely matches two different PSDs with the same β. The flame speed ratio (S_L^*) between the PSD and mono-dispersion remains approximately the same for a particular β at a given equivalence ratio. For a constant β, S_L^* increases as ϕ increases. Considering small values of beta ($\beta < 0.1$), from Fig. 7, the flame speed ratio S_L^* is less than 3%, hence can be treated as a mono-dispersed aerosol.

4.1. Effect of small particles in the PSD

To understand the contribution of the small particles in the PSD, the smallest particles ($d_{p,1}$) in the PSD are removed, and then the discrete averaged particle sizes (bins) are generated with $d_{p,\text{min}}$ of the next smallest particle size maintaining the mean particle size and standard deviation. Figure 11 shows the chosen discrete particle sizes and corresponding frequencies with $d_{p,1} = 3.75$ µm (left) and $d_{p,1} = 17.25$ µm (right) for $d_{p,\text{avg}} = 45$ µm with $\sigma = 15$ µm and the smallest particle sizes in each of these cases are highlighted.

To investigate the effect of the small particles in the PSD, let us look closely at the temperature of the gas and particles of different sizes considering two different PSDs but the same $d_{p,\text{avg}}$ and σ. Figure 12 shows the temperature of gas and particle of different sizes for $d_{p,\text{avg}} = 45$ µm with $\sigma = 15$ µm with $d_{p,\text{min}} = 3.75$ µm (left) and $d_{p,\text{min}} = 25.97$ µm (right) at $\phi = 0.5$. At low equivalence

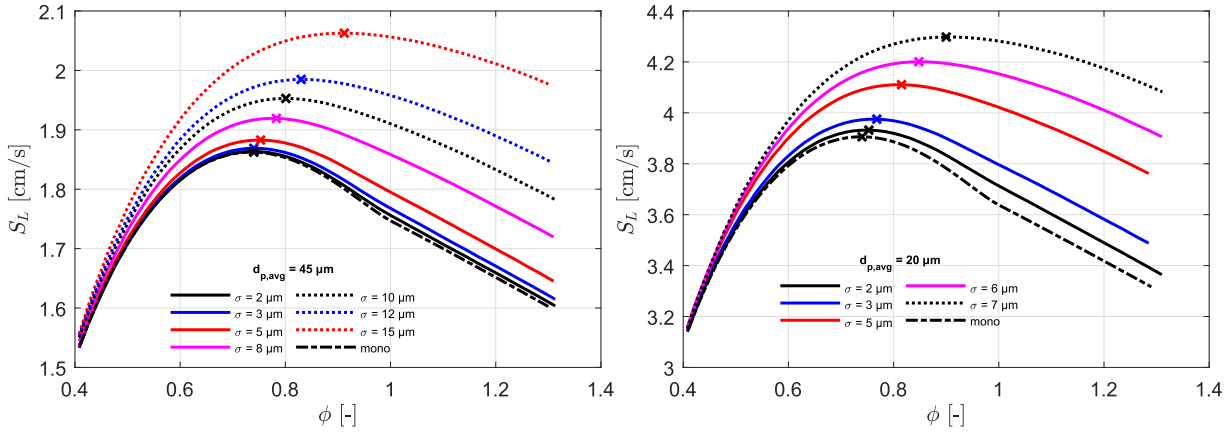

Fig. 7. Flame speed for different σ for $d_p = 45$ µm (left) and $d_p = 20$ µm (right) as a function of equivalence ratio compared against averaged mono-dispersed case; symbols represents the corresponding $\phi_{S_{L,max}}$.

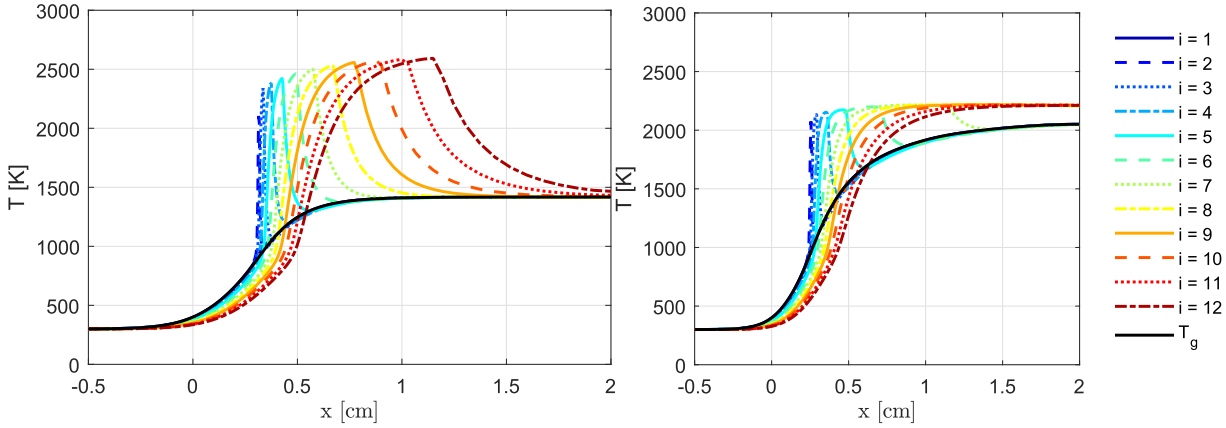

Fig. 8. Temperature of the gas and particles of different diameter for $d_{p,avg} = 45$ µm and $\sigma = 15$ µm for $\phi = 0.5$ (left) and $\phi = 1.0$ (right). The colored profiles represent each particle size from 1 to n_d.

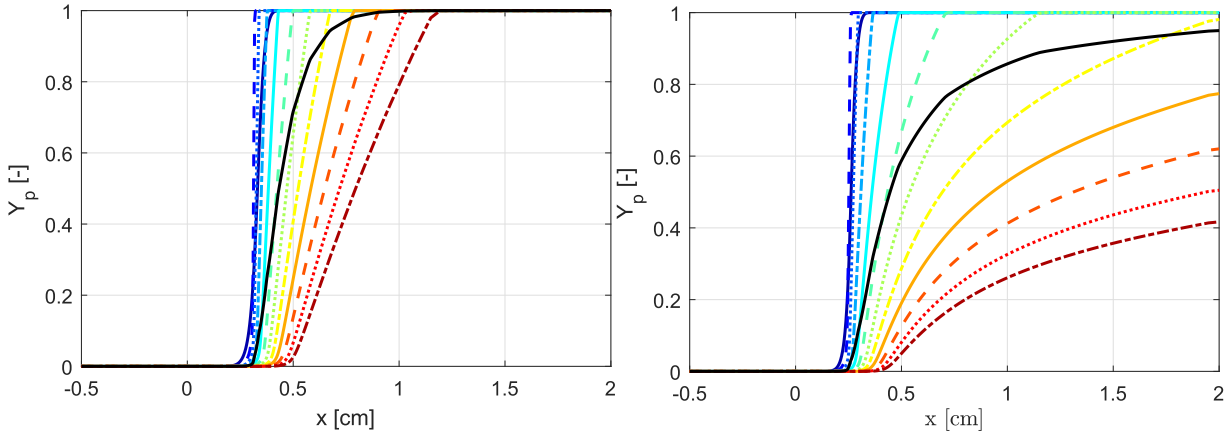

Fig. 9. Burned mass fraction profile for $d_{p,avg} = 45$ µm and $\sigma = 15$ µm for $\phi = 0.5$ (left) and $\phi = 1.0$ (right). Same legend as Fig. 8.

ratios, all the particles have to burn as a whole to sustain a stable flame front. Figure 13 shows the flame structure for $d_{p,avg} = 45$ µm with $\sigma = 15$ µm with $d_{p,min} = 3.75$ µm (left) and $d_{p,min} = 25.97$ µm (right) at $\phi = 1.0$. At high equivalence ratios, not all particle sizes oxidize completely in the computational domain ($Y_p = 1$) as the heating time scales of the small particles are shorter than the big particles. Therefore, the small particles ignite earlier, and the largest particles burn in a region with a rather low oxygen concentration. Eventually, the big particles will oxidize completely because there is sufficient oxygen. It will take a lot of time though and it will happen far downstream. Looking closely at Fig. 13, only half of the particle sizes have reached thermal equilibrium with their gas-phase surrounding while others are still burning. This is clearly visible in Fig. 14, which shows the burned mass fraction of each particle size for $d_{p,avg} = 45$ µm with $\sigma = 15$ µm with $d_{p,min} = 3.75$ µm (left) and the comparison of the average mass fraction profiles between $d_{p,min} = 3.75$ µm and $d_{p,min} = 25.97$ µm (right) at $\phi = 1.0$. When considering $d_{p,min} = 3.75$ µm, the first

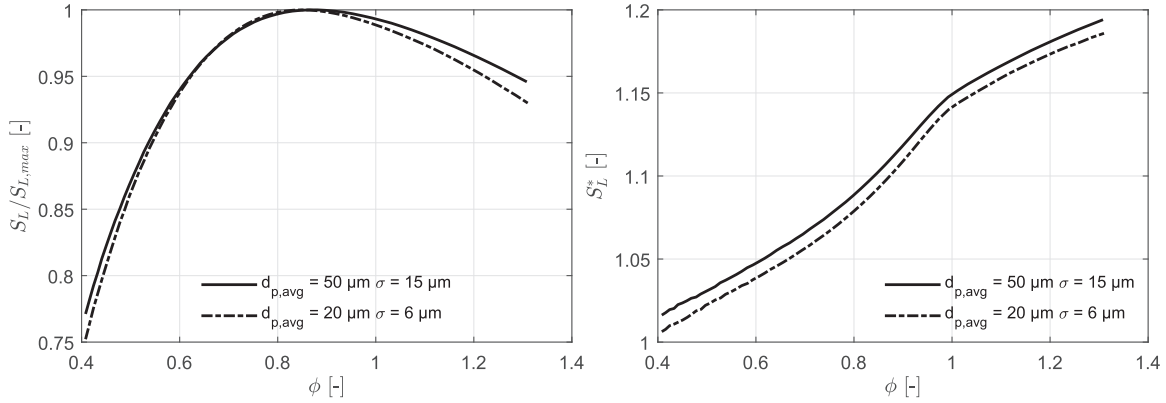

Fig. 10. Normalized flame speed $S_L/S_{L,max}$ (left) and $S_L^* = S_L/S_{L,mono}$ (right) for different $d_{p,avg}$ and σ but same $\beta = 0.3$ against equivalence ratio.

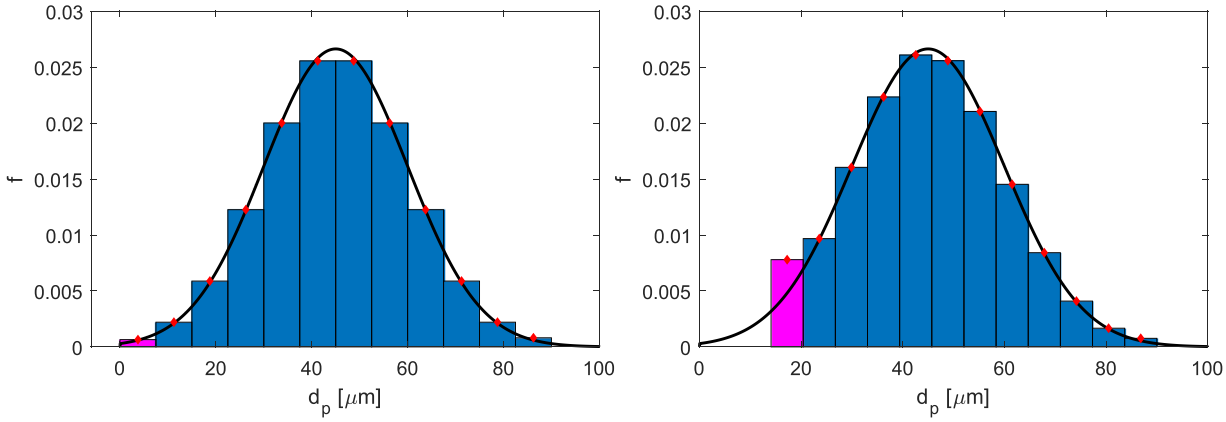

Fig. 11. PSD with $d_{p,1} = 3.75$ µm (left) and PSD with $d_{p,1} = 17.25$ µm (right) for $d_{p,avg} = 45$ µm and $\sigma = 15$ µm.

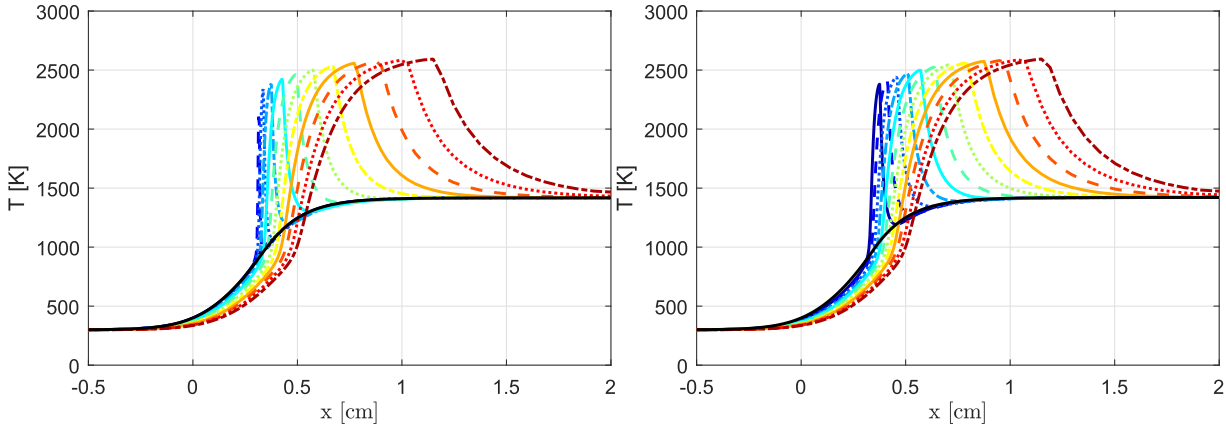

Fig. 12. Temperature of the gas and particles for $d_{p,avg} = 45$ µm and $\sigma = 15$ µm with smallest particle size in the PSD $d_{p,min} = 3.75$ µm (left) and $d_{p,min} = 25.97$ µm (right) at $\phi = 0.5$. Same legend as Fig. 8.

eight particle sizes are completely burned in the computational domain (x = 2cm), and when considering $d_{p,min} = 17.25$ µm, the first six particles sizes are completely burned but $Y_{p,avg}$ is the same.

Figure 15 (left) shows the flame speed for different $d_{p,1}$ as a function of equivalence ratio and the flame speed of the monodispersed case is added for comparison. One might expect that changing the smallest particle size in the PSD can result in a large change in the flame speed. However, the density of the smallest particles ($d_{p,1} = 3.75$ µm) in the dispersion is very low (about 0.4% mass-based) which is not sufficient to increase the gas temperature to the required temperature for the next particle size ($d_{p,2}$) to ignite. Hence, a sufficient amount of small particles is required to increase the gas temperature, thereby igniting the small particles and sustaining a flame front.

When $d_{p,min}$ was changed from the reference value of 3.75 µm to 14.09 µm, the flame speed of the PSD only changed marginally. This implies, that the contribution of the small particles ranging from 3.75 µm to 14.09 µm is negligible at all equivalence ratios. But, when $d_{p,min}$ is changed to 20.28 µm (blue dotted line), the flame speed is lowered and there is a shift in the equivalence ratio at which the maximum flame speed occurs. The flame speed with $d_{p,1} = 20.28$ µm starts to deviate more significantly compared to the reference value for $\phi > 0.8$. This is because, at a low equivalence ratio, the flame speed is dominated by the particle sizes

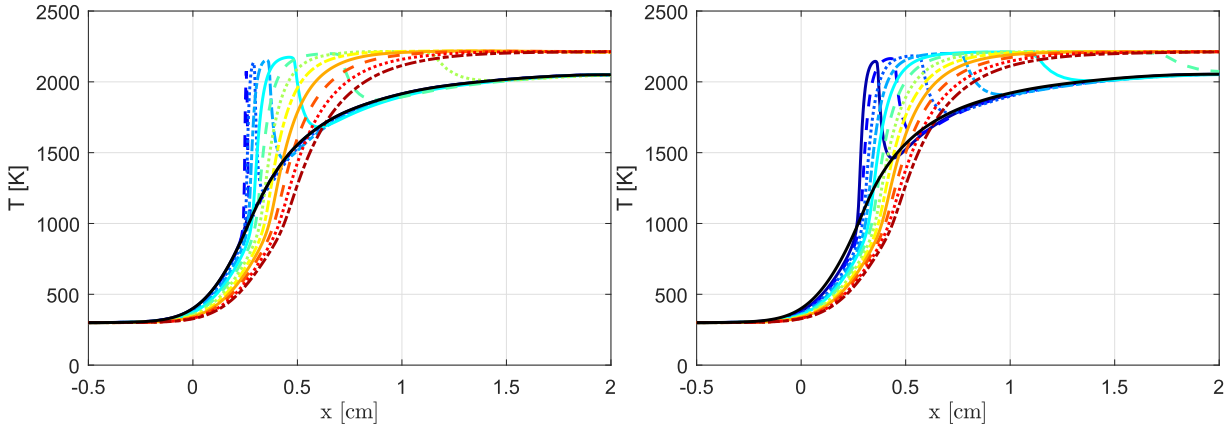

Fig. 13. Temperature of the gas and particles of different diameter for $d_{p,avg} = 45$ µm and $\sigma = 15$ µm for $d_{p,min} = 3.75$ µm (left) and $d_{p,min} = 25.97$ µm (right) at $\phi = 1.0$. Same legend as Fig. 8.

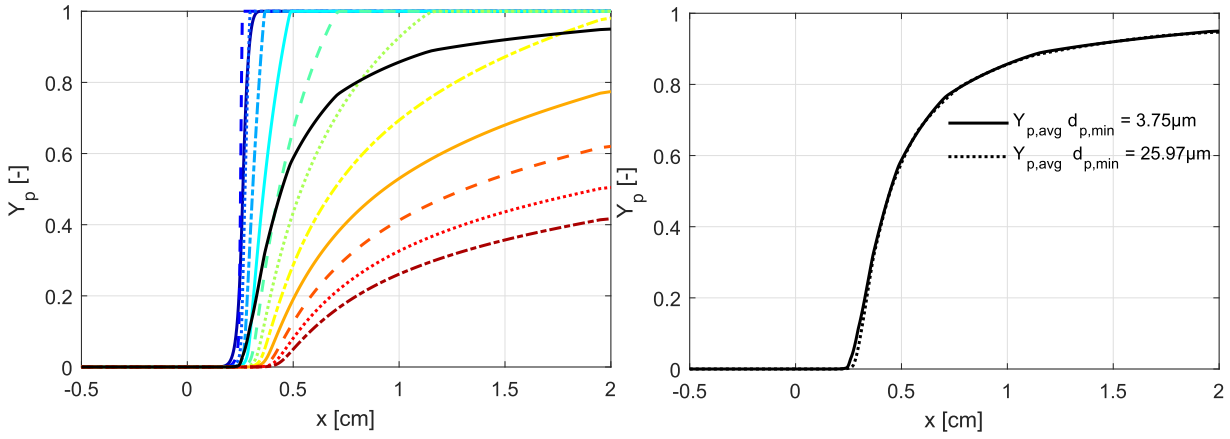

Fig. 14. Burned mass fraction profiles for $d_{p,avg} = 45$ µm and $\sigma = 15$ µm for $d_{p,min} = 3.75$ µm (left) and comparing the average mass fraction profiles between $d_{p,min} = 3.75$ µm and $d_{p,min} = 25.97$ µm (right) at $\phi = 1.0$. Same legend as Fig. 8.

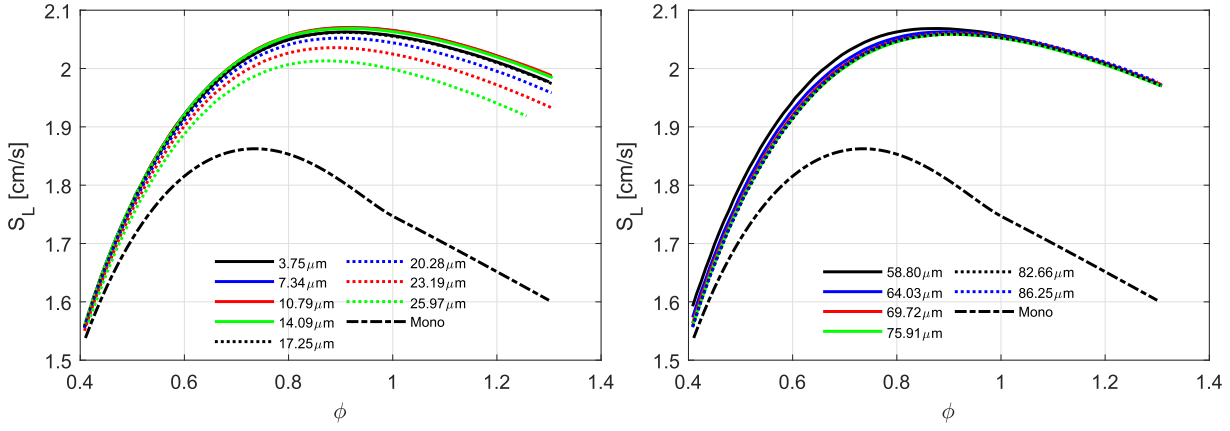

Fig. 15. Flame speed as a function of equivalence ratio for different minimum (left) and maximum (right) particle sizes in the PSD for $d_p = 45$ µm and $\sigma = 15$ µm.

which are closer to the average particle size as the mass fraction of $d_{p,1}$ is very low (less than 10%) compared to the particle sizes near $d_{p,avg}$. As $d_{p,1}$ is further increased, the flame speed further reduces compared to the reference case. For $d_{p,avg} = 45$ µm with $\sigma = 15$ µm, removing the particle sizes lower than 23 µm results in a maximum variation of about 2.5% in the flame speed compared to the reference case. If the mass fraction of small particles ($d_{p,1}$) is too low to sustain a flame front then it cannot enhance the flame speed significantly. For this particular case, the increase in the flame speed at $\phi = 1.0$ was less than 1% between $d_{p,1} = 3.75$ µm and 20 µm. Hence, the inclusion of a small fraction of tiny particles in the PSD is unnecessary to predict the flame speed.

When the mass fraction of particles with a diameter smaller than critical particle size is sufficient to support flame propagation, all these particles will burn nearly simultaneously in a single reaction front. As a consequence, it is possible to represent all these particles with one particle size.

4.2. Effect of big particles in the PSD

Similar to the analysis for the small particles in the previous section, big particles in the PSD are removed in this section. Figure 15 (right) shows the flame speed variation for different $d_{\mathrm{p,max}}$ as a function of equivalence ratio and compared against the mono-dispersed case. The removal of the big particle sizes affects the flame speed marginally because these particle sizes burn slowly compared to the other small particle sizes. Therefore, their heat release occurs mainly far downstream of the flame front.

Considering $d_p = 45$ µm and $\sigma = 15$ µm, the particle sizes from 3.75 µm to 56.25 µm at $\phi = 1.0$ are completely burned within the computational domain but the particle sizes from 63.75 µm to 86.25 µm are not. As the small particle sizes dominate the flame speed due to the short heating time compared to big particle sizes, the big particles would need to heat up in a short time to release their heat in the flame front. From all the simulations performed for different average particle sizes and standard deviations, it was found that the removal of big particles does not affect the flame speed unless the chosen biggest particle size is $d_{\mathrm{p,max}} \lesssim 1.25\, d_{\mathrm{p,avg}}$. This is because the heating time of the big particles is lower than the burning time of the small particles when the size of the big particles is smaller than the critical particle size.

5. Conclusion

Detailed numerical investigations were performed to understand the flame propagation speed and structure of the particle size distribution of iron aerosols. This is a novel study as there were no previous studies to understand the effect of particle size distribution on flame propagation in iron aerosols.

There is a big difference between mono- and poly-dispersed flames. The poly-dispersed flames have a higher flame speed than mono-dispersed flames of the same average particle size and the maximum flame speed of poly-dispersed flames is observed at a higher equivalence ratio than mono-dispersed flames. The difference in the flame speed (S_L^*) between the poly- and mono-dispersed increases as ϕ increases. For $d_{\mathrm{p,avg}} = 45$ µm with $\sigma =$ 15 µm, the flame speed at $\phi = 1.3$ is about 25% higher than the mono-dispersed case. This happens because the flame front is dominated by the burning of small particles and the big particles oxidize slowly in the post-flame region. Varying the standard deviation from low ($\sigma = 2$ µm) to high ($\sigma = 15$ µm) values for the same averaged particle size results in an increase in the flame speed and the location at which maximum flame speed occurs ($\phi_{S_{\mathrm{L,max}}}$). This is a significant finding which can explain why different experimental measurements reported different equivalence ratios at which the maximum flame speed occurs. When the standard deviation changes from low to high values, the variation in heating and burning time scales of the particle sizes increases, resulting in this behavior.

To compare different average particle sizes and standard deviations, a dimensionless standard deviation $\beta = \sigma / d_{\mathrm{p,avg}}$ was introduced. For PSDs with different average particle diameters but similar dimensionless standard deviation, the increase in flame speed compared to the mono-dispersed case is the same. The increase in flame speed gets larger with an increase in the dimensionless standard deviation. This implies that the flame speed becomes more sensitive to the standard deviation of the PSD for smaller average particle diameters. For a standard deviation $\beta < 0.1$, the maximum difference between mono- and poly-dispersed flame speed is less than 3% and hence can be treated as mono-dispersed aerosols.

A detailed investigation of the influence of the small particles in the poly-dispersion shows that when β is high, the density of the smallest particles in the discrete PSD is too small to provide sufficient heat to support a propagating flame front. When the mass fraction of particles with a diameter smaller than critical particle size is sufficient to support flame propagation, all these particles will burn nearly simultaneously in a single reaction front. As a consequence, it is possible to represent all these particles with one particle size. Similarly, for the big particles in the discrete PSD, if the heating time of the big particles is lower than the burning time of the small particles, which occurs when the size of the big particles is smaller than the critical particle size, then the big particles can affect the flame speed. And the particle sizes above the critical particle size can be represented with one particle size. Generally, the flame front speed in the poly-dispersion is controlled by the burning of small particles and the big particles oxidize in the post-flame region thus taking the heat away from the flame front.

The findings of this study are important for the interpretation of flame speed measurements of iron aerosols and other heterogeneously burning dispersion. The conclusions of this study are also valid for PSDs with a shape similar to normal distributions. To demonstrate this, a comparison of flame speed, flame structure, and burned mass fraction profiles of normal and Weibull distributions are added in the supplementary material.

Declaration of Competing Interest

The authors declare that they have no known competing financial interests or personal relationships that could have appeared to influence the work reported in this paper.

Acknowledgments

The authors acknowledge T. Hazenberg for the useful discussion and feedback on this work. The financial support of the Netherlands Organisation for Scientific Research (NWO) under project number 17688 and Opzuid (stimulus) Grant agreement No. PROJ-02594 are gratefully acknowledged.

Supplementary material

Supplementary material associated with this article can be found, in the online version, at doi:10.1016/j.combustflame.2023.113053.

References

[1] J.M. Bergthorson, S. Goroshin, M.J. Soo, P. Julien, J. Palecka, D.L. Frost, D.J. Jarvis, Direct combustion of recyclable metal fuels for zero-carbon heat and power, Appl. Energy 160 (2015) 368–382.
[2] S. Goroshin, M. Bidabadi, J. Lee, Quenching distance of laminar flame in aluminum dust clouds, Combust. Flame 105 (1996) 147–160.
[3] S. Goroshin, M. Kolbe, J.H. Lee, Flame speed in a binary suspension of solid fuel particles, Proc. Combust. Inst. 28 (2000) 2811–2817.
[4] Y. Huang, G.A. Risha, V. Yang, R.A. Yetter, Combustion of bimodal nano/micron-sized aluminum particle dust in air, Proc. Combust. Inst. 31 (2007) 2001–2009.
[5] J. Palecka, S. Goroshin, J.M. Bergthorson, Propagation and quenching of dual-front flames in binary-fuel mixtures, Combust. Sci. Technol. 190 (2018) 1557–1579.
[6] T. Hazenberg, J. van Oijen, Structures and burning velocities of flames in iron aerosols, Proc. Combust. Inst. 38 (2021) 4383–4390.
[7] A. Ravi, P. de Goey, J. van Oijen, Flame structure and burning velocity of flames propagating in binary iron aerosols, Proc. Combust. Inst. (2022), doi:10.1016/j.proci.2022.07.031.
[8] D. Ning, Y. Shoshin, J. van Oijen, G. Finotello, L. de Goey, Burn time and combustion regime of laser-ignited single iron particle, Combust. Flame 230 (2021) 111424.
[9] D.A. Frank-Kamenetskii, N. Thon, Diffusion and heat exchange in chemical kinetics, Princeton University Press, 1955.
[10] A.L. Breiter, V. Mal'tsev, Popov, Models of metal ignition, Combust. Explos. Shock Waves (1977), doi:10.1007/BF00744795.
[11] L. Somers, The simulation of flat flames with detailed and reduced chemical models, Mechanical Engineering, 1994 Ph.D. thesis.
[12] F.L. Sacomano Filho, N. Speelman, J.A. van Oijen, L.P.H. de Goey, A. Sadiki, J. Janicka, Numerical analyses of laminar flames propagating in droplet mists using detailed and tabulated chemistry, Combust. Theory Model. 22 (5) (2018) 998–1032, doi:10.1080/13647830.2018.1470332.

[13] L.C. Thijs, C.E.A.G. van Gool, W.J.S. Ramaekers, J.G.M. Kuerten, J.A. van Oijen, L.P.H. de Goey, Improvement of heat- and mass transfer modeling for single iron particles combustion using resolved simulations, Combust. Sci. Technol. 0 (0) (2022) 1–17, doi:10.1080/00102202.2022.2089030.
[14] L. Thijs, C. van Gool, W. Ramaekers, J. van Oijen, L. de Goey, Resolved simulations of single iron particle combustion and the release of nano-particles, Proc. Combust. Inst. (2022), doi:10.1016/j.proci.2022.07.044.
[15] J. Palečka, J. Sniatowsky, S. Goroshin, A.J. Higgins, J.M. Bergthorson, A new kind of flame: observation of the discrete flame propagation regime in iron particle suspensions in microgravity, Combust. Flame 209 (2019) 180–186, doi:10.1016/j.combustflame.2019.07.023.
[16] N. Poletaev, M. Khlebnikova, Combustion of iron particles suspension in laminar premixed and diffusion flames, Combust. Sci. Technol. 0 (0) (2020) 1–22, doi:10.1080/00102202.2020.1812588.
[17] J.-H. SUN, R. DOBASHI, T. HIRANO, Combustion behavior of iron particles suspended in air, Combust. Sci. Technol. 150 (1–6) (2000) 99–114, doi:10.1080/00102200008952119.
[18] S. Goroshin, I. Fomenko, J.H. Lee, Burning velocities in fuel-rich aluminum dust clouds, Symp. (Int.) Combust. 26 (2) (1996) 1961–1967, doi:10.1016/S0082-0784(96)80019-1.
[19] J.-H. Sun, R. Dobashi, T. Hirano, Structure of flames propagating through metal particle clouds and behavior of particles, Symp. (Int.) Combust. 27 (2) (1998) 2405–2411, doi:10.1016/S0082-0784(98)80092-1.